npj computational materials

www.nature.com/npjcompumats

ARTICLE OPEN

Check for updates

Superconductivity and topological aspects of two-dimensional transition-metal monohalides

Wen-Han Dong[1,2], Yu-Yang Zhang[2,3], Yan-Fang Zhang[2], Jia-Tao Sun[4], Feng Liu[5]✉ and Shixuan Du[1,2,3,6]✉

Two-dimensional (2D) superconducting states have attracted much recent interest, especially when they coexist with nontrivial band topology which affords a promising approach towards Majorana fermions. Using first-principles calculations, we predict van der Waals monolayered transition-metal monohalides *MX* (M = Zr, Mo; X = F, Cl) as a class of 2D superconductors with remarkable transition temperature (5.9–12.4 K). Anisotropic Migdal-Eliashberg theory reveals that ZrCl have a single superconducting gap $\Delta \sim 2.14$ meV, while MoCl is a two-gap superconductor with $\Delta \sim 1.96$ and 1.37 meV. The Z_2 band topology of 2D *MX* is further demonstrated that MoF and MoCl are candidates for realizing topological superconductivity. Moreover, the Dirac phonons of ZrCl and MoCl contribute w-shape phononic edge states, which are potential for an edge-enhanced electron-phonon coupling. These findings demonstrate that 2D *MX* offers an attractive platform for exploring the interplay between superconductivity, nontrivial electronic and phononic topology.

npj Computational Materials (2022)8:185 ; https://doi.org/10.1038/s41524-022-00871-y

INTRODUCTION

Two-dimensional (2D) superconductivity, which may occur in heterogeneous interfaces and atomic-thin layers, has attracted growing attention because of its fundamental interest and practical application[1]. Over the past decade, the advent of nanofabrication methods, such as molecular beam epitaxy and mechanical exfoliation[2], has enabled the exploration of ultrathin and highly crystalline 2D superconductors[3–6], and intriguing phenomena have been unveiled, such as quantum Griffiths singularity[7,8], anomalous/bosonic metallic state[9] and enhanced upper critical field[6,10]. Some 2D superconductors can achieve much higher superconducting transition temperature T_c than their bulk counterparts, such as the FeSe/$SrTiO_3$ interface[11,12] and surface-hydrogenated monolayer MgB_2[13]. Especially, monolayer T_d-$MoTe_2$ was discovered to have a 60-times T_c enhancement (~7.6 K) over the bulk phase (~0.1 K) by electrical gating[14].

In general, practical application of 2D superconductors has to include the effect of substrate, which may suppress the superconductivity[15,16] in particular the high T_c predicted, such as 24.7 K for borophene[17]. In this regard, van der Waals (vdW) layered materials are obviously advantageous. Representatively, the transition metal dichalcogenides (TMDs) have provided a fertile land for 2D superconductivity. For example, the coexistence of superconductivity and charge density wave phases in 2H-$NbSe_2$[18,19], two types of Ising pairing in gated 2H-MoS_2 and 1T_d-$PdSe_2$[10,20,21], and metastable superconductivity of $IrTe_2$[22]. 2M-WS_2 presents the highest $T_c = 8.8$ K among intrinsic TMDs[23]. Beyond TMDs (atomic layers $N = 3$), recent computational studies have predicted a high $T_c \sim 21$ K in monolayer W_2N_3 ($N = 5$)[24,25].

More interestingly, when superconductivity meets with nontrivial band topology[26], their interplay can lead to more exotic topological superconducting (TSC) state, e.g., manifesting in Majorana fermionic mode, which offers quantum computing with high fidelity of fault tolerance[27]. In addition to interfacing superconducting and topological states in heterostructures by superconducting proximity effect[28,29] or Berezenskii-Kosterlitz-Thouless phase transition[30], the coexistence of superconducting and topological states offers a promising platform for realizing Majorana fermions without complex interface conditions[25]. Efforts have been made by searching either superconducting state in a topological material[31–35] or conversely topological state in a superconductor[36,37]. Excitingly, a recent experiment has evidenced the Majorana bound states in superconducting 2M-WS_2[38]. Besides TSC, the additional electronic and phononic states at surface or edge can play a significant role of reinforcing electron-phonon coupling (EPC) and superconductivity by interacting with bulk phonons or electrons[39,40]. For instance, the nontrivial topological states on Be (0001) surface give rise to an anomalously large surface EPC[41]. Given these aspects, it is fundamentally interesting to explore 2D superconductors with electronic and phononic topology.

In this paper, we report the investigation of superconductivity and topological aspects of vdW-monolayered *MX* (M = Zr, Mo; X = F, Cl) based on first-principles calculations. 2D *MX* have strong EPC ($\lambda > 1$) and remarkable T_c (5.9–12.4 K) due to the softening of acoustic phonon modes. Anisotropic Migdal-Eliashberg theory unveils that monolayer ZrCl is a single-gap superconductor with $T_c \sim 12.4$ K and superconducting gap $\Delta_0 = 2.14$ meV, higher than the predicted 1.5 meV of 2M-WS_2[42]. Monolayer MoCl displays a distinct two-gap superconductivity. And the larger gap $\Delta_0 = 1.96$ meV has a ratio $2\Delta_0/k_BT_c = 4.69 > 3.53$, exhibiting a strong coupling beyond the Bardeen-Cooper-Schrieffer (BCS)[43] superconductors. In addition, 2D *MX* are encoded with the Z_2 band topology, and monolayer MoF, MoCl are TSC candidates. We also identify the Dirac phonons of monolayer ZrCl and MoCl with quantized $\pm\pi$ Berry phases at Brillouin zone boundaries. Corresponding zigzag edge states display w-shape dispersions, indicating a potential edge-enhanced EPC in the one-dimensional zigzag

[1]Beijing National Center for Condensed Matter Physics and Institute of Physics, Chinese Academy of Sciences, Beijing 100190, China. [2]School of Physical Sciences, University of Chinese Academy of Sciences, Beijing 100049, China. [3]CAS Center for Excellence in Topological Quantum Computation, Beijing 100190, China. [4]School of Integrated Circuits and Electronics, MIIT Key Laboratory for Low-Dimensional Quantum Structure and Devices, Beijing Institute of Technology, Beijing 100081, China. [5]Department of Materials Science and Engineering, University of Utah, Salt Lake City, Utah 84112, USA. [6]Songshan Lake Materials Laboratory, Dongguan 523808, China. ✉email: fliu@eng.utah.edu; sxdu@iphy.ac.cn

ribbons of ZrCl and MoCl. Our results demonstrate the intriguing superconducting and topological properties in 2D *MX*, deserving further experimental verifications.

RESULTS

Atomic and electronic structures

As shown in Fig. 1a, our investigated vdW-monolayered transition-metal monohalides *MX* (M = Zr, Mo; X = F, Cl) have a 1:1 *X-M-M-X* sandwich structure with $P\bar{3}m1$ symmetry (No. 164), where top and bottom sub-monolayers constitute two sublattices (pseudospins) in Bernal stacking. Bulk ZrCl has been synthesized in 1970s by reacting gas phase $ZrCl_4$ with abundant electropolished Zr[44,45]. Similar synthetic method should be applicable to bulk MoCl, MoF and ZrF. For example, one may obtain MoF by reacting Mo with MoF_6 gas[46]. The calculated binding energy is 17.1 meV Å^{-2} for ZrCl, 26.2 meV Å^{-2} for MoCl, 16.0 meV Å^{-2} for ZrF and 28.4 meV Å^{-2} for MoF, respectively, including the vdW-D3 correction[47]. The results of binding energy are close to known vdW-monolayers like 2H-MoS_2 (23.7 meV Å^{-2})[48], indicating our proposed monolayer *MX* can be mechanically exfoliated from the bulk.

Band structures in Fig. 1b, c, Supplementary Figs. 2a and 3a show that 2D *MX* are metallic with two spin-degenerate bands (α for hole-like and β for electron-like) crossing the Fermi level. Here, we focus on monolayer ZrCl, MoCl since monolayer ZrF, MoF exhibit similar electronic structures, respectively. The Fermi surface (FS) of monolayer ZrCl consists of one hole pocket FS1 and two electron pockets FS2, FS3 centered at Γ point (Fig. 3a), while that of monolayer MoCl has one flower-shaped hole pocket FS2 near Brillouin zone boundaries and one electron pocket FS1 at Γ point (Fig. 3d). Notably, the FS2 of monolayer MoCl is slightly different that the in-plane $d_{x^2-y^2,xy}$ orbitals dominate near K point and out-of-plane d_{z^2} orbital dominates near M point. The density of states (DOS) of monolayer ZrCl and MoCl are both about peaking at the Fermi level, with $N(E_F)$ equals to 2.78 states eV^{-1} and 1.71 states eV^{-1}, respectively.

Superconductivity in 2D *MX*

We first show the phonon dispersions of 2D *MX* in Fig. 2a, c, Supplementary Figs. 2c and 3c. To investigate the EPC, we have calculated the Eliashberg function $\alpha^2F(\omega)$ and accumulated EPC coefficient $\lambda(\omega)$ in Fig. 2b, d, Supplementary Figs. 2d and 3d. As listed in Table 1, 2D *MX* all have a strong integral EPC coefficient $\lambda > 1$. Monolayer ZrCl exhibits the highest McMillan-Allen-Dynes[49] $T_c = 12.0$ K ($\mu^* = 0.1$). Notably, the low-frequency phonons (< 150 cm^{-1}) of 2D *MX* contribute mostly to the EPC. In particular, the mode-1 of monolayer ZrCl and mode-2, mode-3 of monolayer MoCl are acoustic soft modes hosting considerable weights of $\lambda_{\mathbf{q}\nu}$ (Fig. 2a, c). These soft modes prefer to form attractive electron-phonon interaction and contributes to the $\alpha^2F(\omega)$ peaks (Fig. 2b, d). We have also estimated their significant contributions to the enhancement of total EPC λ. It shows that mode-1 contributes 23% of λ of monolayer ZrCl, mode-2 and mode-3 together contribute 36% of λ of monolayer MoCl (Supplementary Note 2). We will discuss the origin of these soft modes in the section below.

Moreover, we have analyzed the EPC-favorable vibration modes in 2D *MX* (Fig. 2e–g and Supplementary Fig. 2e, f). Interestingly for monolayer ZrCl, the soft mode-1 at K point is mainly from Zr atoms that vibrate circularly but of opposite chirality between top and bottom sub-monolayers (Fig. 2e). The previous study[50] reveals that chiral-phonon modes can be induced by breaking the inversion symmetry of monolayer ZrCl. Based on this, we have explored the Janus structure of monolayer Zr_2FCl ($P3m1$ symmetry, No.156) in Supplementary Fig. 4. We find there are two chiral-phonon-related $\alpha^2F(\omega)$ peaks in monolayer Zr_2FCl, and the predicted T_c is further enhanced to 13.2 K. Particularly in Supplementary Fig. 4c, one finds the lowest phonon branch seems to develop a roton-like minimum at the K valley. It may originate from the phonon-chirality-induced attractive intervalley dipole-dipole interaction, reminiscent of the roton mode in a BEC experiment[51]. Roton is a kind of quasiparticle first introduced to explain the spectrum of superfluid ^{4}He. In a recent study[52], it is also found the chiral modes can cause a roton-like minimum in the acoustic phonon branch. We believe this finding may help better understanding the relation between chiral phonon and superconductivity: when the chiral modes appear in the acoustic

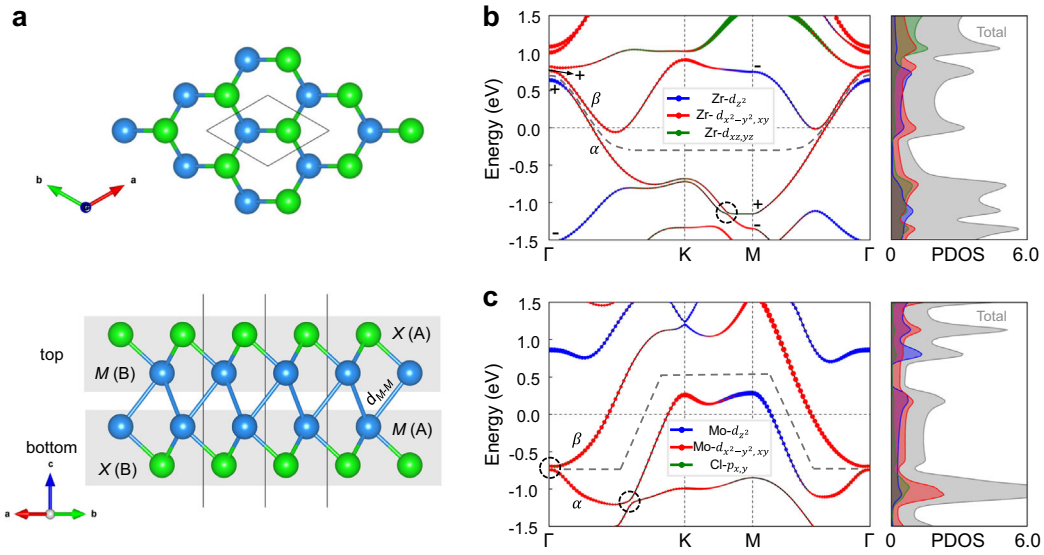

Fig. 1 Atomic and electronic structures. a Crystal structure of monolayer transition-metal monohalides *MX* (M = Zr, Mo; X = F, Cl) with two (top and bottom) *M-X* sub-monolayers. Orbital-weighted band structures with spin-orbit coupling (SOC) and projected density of states (DOS) of **b** monolayer ZrCl and **c** monolayer MoCl. Here, + (−) denote parities. The two bands with crossing the Fermi level are labeled as α and β. The gray dashed lines exhibit the curved Fermi level, and the black dashed circles show SOC gaps at Dirac-type crossings (i.e., crossing points without SOC).

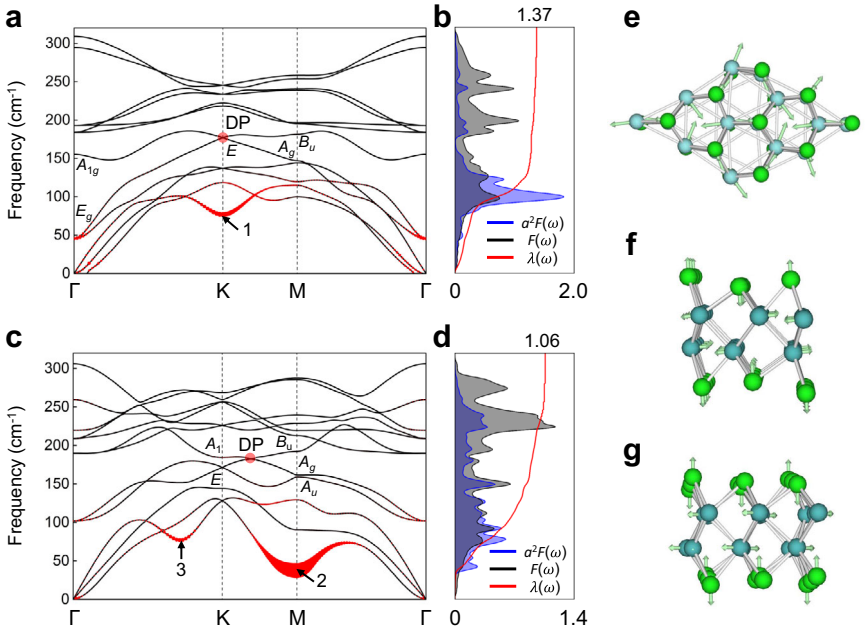

Fig. 2 Phonon properties and EPC. a Phonon dispersion of monolayer ZrCl and **b** its Eliashberg function $\alpha^2F(\omega)$, phonon DOS $F(\omega)$ and accumulated EPC coefficient $\lambda(\omega)$. **c** Phonon dispersion of monolayer MoCl and **d** its $\alpha^2F(\omega)$, $F(\omega)$ and $\lambda(\omega)$. In **a** and **c**, the red weighted dots display momentum-mode resolved $\lambda_{\mathbf{q}\nu}$ by magnitude. The Dirac points (DPs) and acoustic soft modes at point 1, 2 and 3 are also marked. **e** Schematic of the vibration mode of monolayer ZrCl at point 1 with frequency 75.8 cm^{-1}, where Zr atoms in the top (bottom) sub-monolayer vibrate circularly left-handed (right-handed), as indicated by the arrows. Schematics of the vibration modes of monolayer MoCl **f** at point 2 with frequency 37.1 cm^{-1} and **g** at point 3 (along Γ–K path) with frequency 77.1 cm^{-1}.

Table 1. Structural, superconducting and topological properties of 2D *MX* (*M* = Zr, Mo; *X* = F, Cl).

Formula	*a* (Å)	$d_{M\text{-}M}$ (Å)	λ	T_c (K)	Z_2	TSC candidate	Phononic DP
ZrCl	3.35	3.17	1.37	12.4 (A-ME) 12.0 (MAD)	1	No	176.8 cm^{-1}, 2DPs
MoCl	3.16	2.59	1.06	9.7 (A-ME) 10.1 (MAD)	1	Yes	183.2 cm^{-1}, 6DPs
ZrF	3.14	3.12	1.03	10.5 (MAD)	1	No	No
MoF	2.92	2.59	1.27	5.9 (MAD)	1	Yes	No

The second, third and fourth columns show lattice constant *a*, nearest *M*-*M* bond length $d_{M\text{-}M}$ and EPC constant λ. T_c was estimated by either anisotropic Migdal-Eliashberg (A-ME) theory[53] or McMillan-Allen-Dynes (MAD) formula[49] with $\mu^* = 0.1$. Z_2 invariant of electronic topology was obtained by symmetry-indicator thoery[64]. The frequency and number of phononic Dirac point (DP) are given in the last column.

phonon branches, they may accelerate the so-called roton-like phonon softening, which in turn enhances EPC and superconductivity.

We have also employed Migdal-Eliashberg theory[53] to obtain the finite-temperature superconducting properties. The estimated T_c of monolayer ZrCl and MoCl by anisotropic Migdal-Eliashberg theory are close to those from McMillan-Allen-Dynes formula (Table 1), while the isotropic Migdal-Eliashberg approximation leads to a ~20% overestimation of T_c (Supplementary Fig. 6). In Fig. 3b, monolayer ZrCl is found to have an averaged superconducting gap vanishing at $T_c = 12.4$ K and three FS sheets jointly contributing to a single-gap distribution with median EPC strength[53] $\lambda^{el}_{n\mathbf{k}} \sim 1.35$. Such single-gap nature is also captured by the normalized quasiparticle DOS in Fig. 3c. The superconducting gap of monolayer ZrCl at zero temperature limit is $\Delta_0 = 2.14$ meV, yielding a ratio $2\Delta_0/k_BT_c = 4.00 > 3.53$ of BCS value. The one-gap α-model fitting[54] of the averaged superconducting gap with $\Delta(T)/\Delta_0 = (1 - (T/T_c)^p)^{0.5}$ gives $p = 3.4$. In addition, monolayer MoCl exhibits a distinct two-gap superconductivity with $T_c = 9.7$ K and two peaks in the normalized quasiparticle DOS (Fig. 3e, f). The multigap superconductivity was first discovered in MgB_2, where the two superconducting gaps are respectively from σ and π FS sheets[55]. Based on FS analysis, we find the spin textures of FS2 of monolayer MoCl are spirally flipped due to the aforementioned in-plane and out-of-plane orbital compositions, quite different from that of FS1 (Fig. 3d). We attribute the two-gap superconductivity to the well-separated FS1 and FS2 of monolayer MoCl. Since the cross pairings between bands with different orbital components are energetically disfavored, it further leads to the two-component $\lambda^{el}_{n\mathbf{k}}$ distribution in the inset of Fig. 3e. Notably, the large superconducting gap $\Delta_{\beta 0} = 1.96$ meV displays a significant Cooper pairing with the ratio $2\Delta_{\beta 0}/k_BT_c = 4.69 > 3.53$. While the small gap $\Delta_{\alpha 0} = 1.37$ meV has the ratio $2\Delta_{\alpha 0}/k_BT_c = 3.28$ (close to 3.53). The two-gap α-model fitting $\Delta_{\alpha,\beta}(T)/\Delta_{(\alpha,\beta)0} = (1 - (T/T_c)^p)^{0.5}$ gives $p = 2.8$. Given the two-gap feature, several intriguing superconducting phenomena, such as anisotropy of the upper critical field[56], are anticipated in monolayer MoCl.

EPC mechanisms

Here we explain the origins of acoustic soft modes in monolayer ZrCl and MoCl. Phonon softening can originate from mechanisms of either FS nesting[57] or incipient/latent lattice instability under fluctuations[58]. The latter mechanism happens when the Fermi

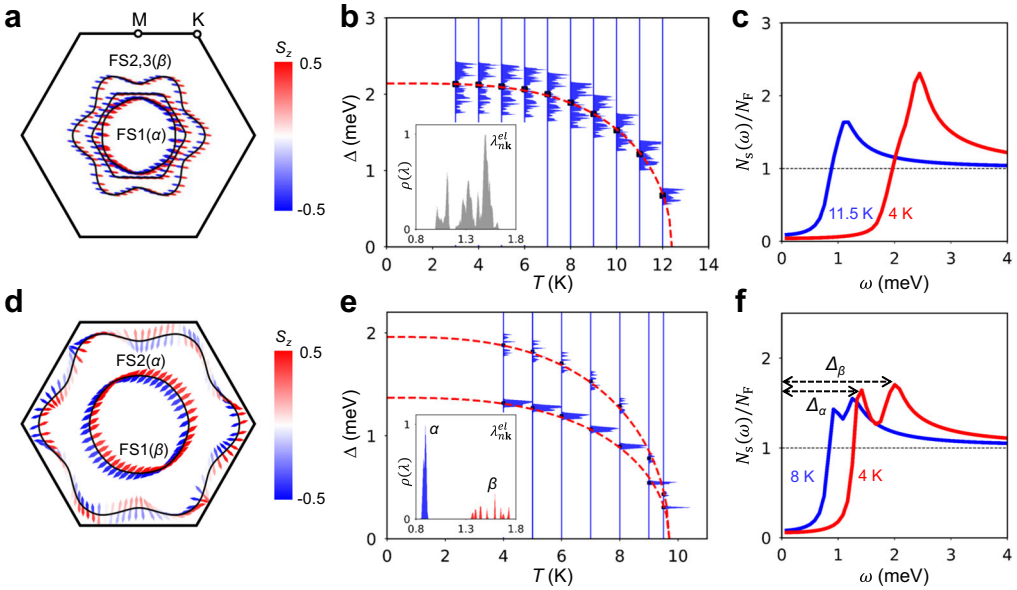

Fig. 3 Superconducting properties. a Fermi surface (FS) with in-plane spin textures of monolayer ZrCl. The arrows show the in-plane spin orientations and the opposite spins at **k** and −**k** points are anti-parallel, indicating a spin-singlet *s*-wave pairing. **b** Temperature-dependent superconducting gap distribution of monolayer ZrCl based on anisotropic Migdal-Eliashberg theory. The red dashed line in **b** represents α-model fitting using the average gap values (black square dots) and the inset is the density distribution of EPC strength $\lambda^{el}_{n\mathbf{k}}$. **c** Normalized superconducting quasiparticle DOS of monolayer ZrCl at 4 K and 11.5 K. **d**–**f** FS with in-plane spin texture, temperature-dependent superconducting gap distribution, and normalized superconducting quasiparticle DOS of monolayer MoCl, respectively.

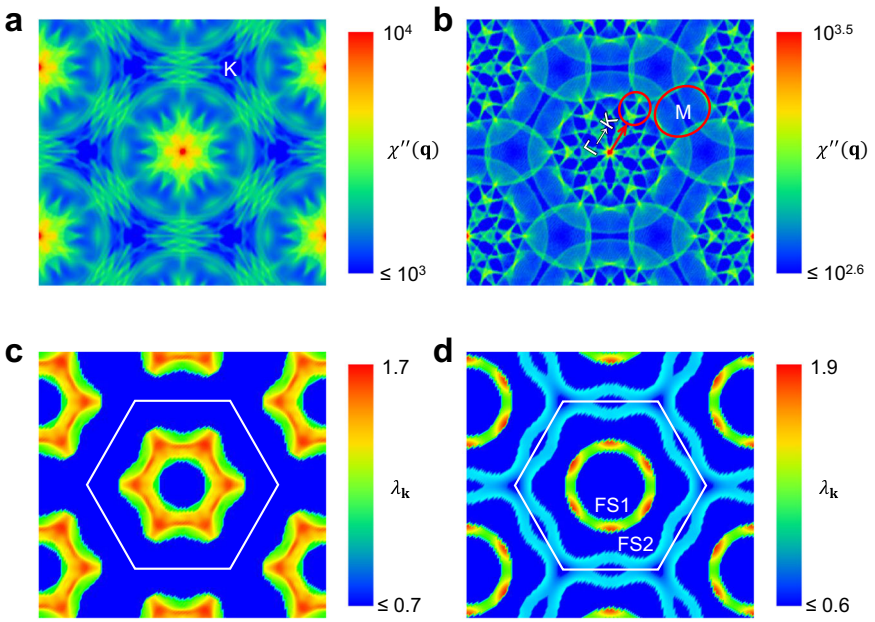

Fig. 4 Unveiling the EPC mechanisms. FS nesting function $\chi''(\mathbf{q})$ of **a** monolayer ZrCl and **b** monolayer MoCl. Notice the peaks at Γ point are irrelevant to the nesting. Electronic EPC strength $\lambda_{\mathbf{k}}$ of **c** monolayer ZrCl and **d** monolayer MoCl near Fermi level (within $E_F \pm 0.2$ eV) at 6 K.

level is near electronic singularities, and the fluctuations cause prominent phonon softening through electron-phonon interaction[59,60]. For monolayer ZrCl, we first rule out the FS nesting effect as the origin of soft mode-1 in Fig. 2a because there is no direct $\chi''(\mathbf{q})$ nesting peak at K point (Fig. 4a). Instead, we notice in Fig. 1b that the DOS peak is very close to Fermi level (0.03 eV lower), suggesting the possibility of the second mechanism. So, following the approach in ref. [60], we have constructed a 3×3 supercell to examine the possible phonon softening at K point (Supplementary Fig. 9a). We find the frozen A_{1g} mode related lattice fluctuations can indeed lift the electronic degeneracies and consequently reduce electronic densities close to the Fermi level, as shown in Supplementary Fig. 9b–e. It indicates the electronic states couple strongly to phonons at K point in the way analogous to the dynamical Jahn-Teller effect[60], manifesting strong electron-phonon interaction. This is consistent with the mechanism of latent lattice instability[58] for enhancing EPC through softening of mode-1 at K point. For monolayer MoCl, the nesting vector along Γ–K path is marked red in Fig. 4b. Corresponding FS nesting directly leads to the phonon softening of mode-3 in Fig. 2c.

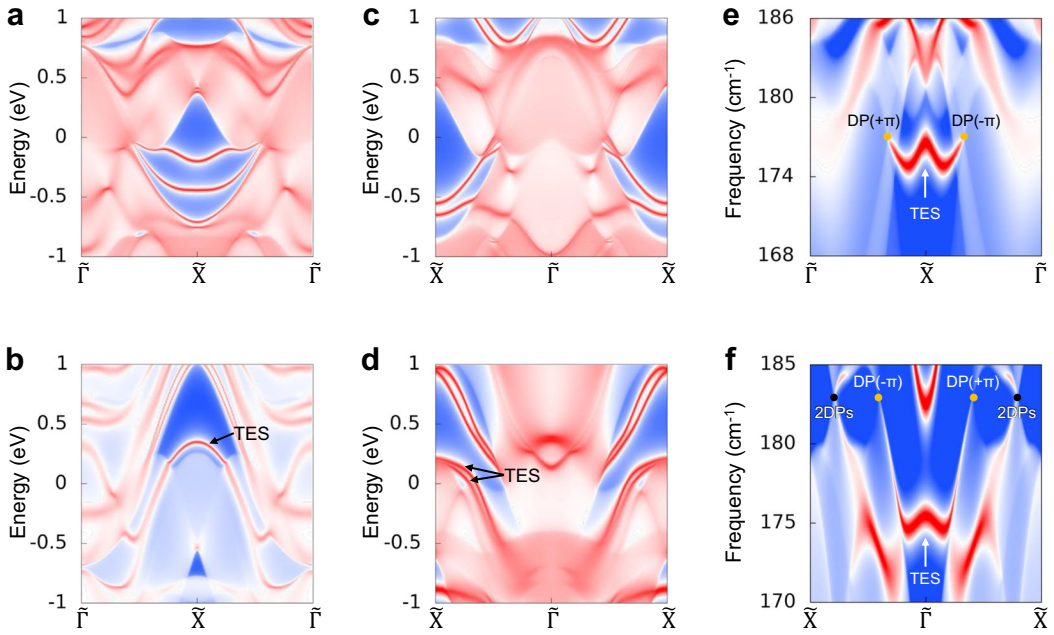

Fig. 5 Electronic and phononic topology in 2D *MX*. The zigzag electronic spectra of **a** ZrCl, **b** MoCl, **c** ZrF and **d** MoF. Here, the nontrivial topological edge states (TESs) in between α and β bands are labeled. The phononic spectra near DPs of **e** ZrCl along zigzag edge and **f** MoCl along zigzag edge. Here, the bulk projected DPs are marked with dots. The golden ones exhibit nontrivial Berry phases of $\pm\pi$, while the black ones are projected from two DPs, having trivial Berry phases of $\pm 2\pi$. Notice the marked TESs have w-shape dispersions and connect to the nontrivial projected DPs.

Also, we find several small and broad nesting peaks around M point, indicating that the soft mode-2 in Fig. 2c arises possibly from phonon renormalization caused by Kohn anomaly[61].

We then study the FS resolved EPC of monolayer ZrCl and MoCl, by inspecting the electronic EPC strength $\lambda_{\mathbf{k}}$[62] in Fig. 4c, d. We have considered a FS spread of 200 meV under 6 K, so that all phonon contributions are taken into account. For monolayer ZrCl, the three FS sheets overlap due to the energy spread (Fig. 4c). The hot spots form a closed hexagon, and the maximal $\lambda_{\mathbf{k}} = 1.66$ appear long Γ–K directions. For monolayer MoCl, the $\lambda_{\mathbf{k}}$ hot spots appear along Γ-M directions of FS1, with a maximal value of 1.86 (Fig. 4d). One can clearly see the phonons are inclined to create strong electron-phonon interaction with FS1. The significant difference between EPC strengths of FS1 and FS2 eventually leads to the two-gap superconductivity as observed in Fig. 3e.

Electronic topology

Besides superconductivity, we have investigated the band topology in 2D *MX*. Strictly speaking, topological insulator state is defined with a global gap for the calculation of Z_2 topological invariants. However, one may loosely calculate an effective Z_2 using a "curved" Fermi level to identify a topological metal[63]. Accordingly, we have calculated the effective Z_2 of 2D *MX* based on symmetry-indicator thoery[64]. Consequently, 2D *MX* all have an effective $Z_2 = 1$ up to both α band and the band following below by assuming a "curved" Fermi level (see Fig. 1b, c). As shown in Fig. 1b, c, Supplementary Figs. 2a and 3a, the band topology of 2D *MX* originates from Dirac-type crossings under Fermi level, at which spin-orbit coupling open the nontrivial gaps. The electronic edge spectra of 2D *MX* along both zigzag and armchair edges are explored in Fig. 5 and Supplementary Fig. 5. We find the zigzag termination is advantageous for observing edge states. In Fig. 5a–d of the zigzag edge spectra, there exist several edge states around the Fermi level. However, only monolayer MoCl and MoF exhibit topological edge states (TESs) with distinct bulk-edge correspondence from the topology between the α and β bands. For monolayer ZrCl and ZrF, the edge states near Fermi level come from bands below α band, which are trivial for realizing TSC. All these indicate monolayer MoCl and MoF are TSC candidates with the coexistence of nontrivial TESs and spin-singlet *s*-wave superconductivity. One promising approach for triggering (helical) TSC states in monolayer MoCl or MoF is to induce Rashba-type band splitting by applying an electrical field[65] and adjust the chemical potential by electrical gating[33].

Phononic topology

The nontrivial phononic topology of monolayer ZrCl and MoCl can be identified in Fig. 2a, c. The phonon dispersions show that monolayer ZrCl possesses two crossing points at the K and K′ valleys, and monolayer MoCl possesses six crossing points along M-K paths. We have calculated the Berry phase of each crossing point by $\gamma = \sum_{n\in \mathrm{occ}} \oint_L A_n(\mathbf{q}) \cdot d\mathbf{q}$[66], where $A_n(\mathbf{q}) = i\langle u_n(\mathbf{q})|\nabla_{\mathbf{q}}|u_n(\mathbf{q})\rangle$ is the Berry connection of the nth phonon branch. We find the crossing points of monolayer ZrCl at 176.8 cm^{-1} and the crossing points of monolayer MoCl at 183.2 cm^{-1} have Berry phases of $\pm\pi$, evidencing they are Dirac phonons. The detailed Berry phase distributions of these Dirac phonons are available in Supplementary Fig. 11. Here we briefly explain the symmetry mechanism. These monolayers are in a $P\bar{3}m1$ symmetry, whose symmetry operations follow D_{3d} point group. All the symmetry-allowed band crossings, i.e., 2D Dirac points (DPs), are discussed in Supplementary Note 9. Importantly, these DPs are protected by the joint $\mathcal{PT}$ symmetry ($\mathcal{P}$: inversion, $\mathcal{T}$: time-reversal), and are pair-related by $\mathcal{T}$: $\mathbf{q} \leftrightarrow -\mathbf{q}$. For monolayer ZrCl, the DP at K (K′) valley is guaranteed by a 2D irreducible representation E, which is C_{3z}-symmetric. For monolayer MoCl, the six DPs (three pairs) along M-K paths are symmetry-allowed accidental crossings, with opposite eigenvalues of in-plane two-fold rotations (see irreducible representations marked in Fig. 2c).

We have also investigated the phononic edge spectra with both zigzag and armchair edge terminations in Supplementary Fig. 11. Interestingly, we discover one w-shape TES for both monolayer ZrCl and MoCl along zigzag edges (Fig. 5e, f). For MoCl in Fig. 5f, the six bulk DPs are projected into two groups: (1) two golden marked projected DPs from one bulk DP, which are topologically nontrivial; (2) two black marked projected DPs from two bulk DPs, which are trivial with total Berry phases of $+2\pi$ and -2π. This point is explained in Supplementary Fig. 11d. Here, the w-shape TES only connects to the nontrivial projected DPs. If the two trivial projected DPs are connected, there will be two edge states from the same start point to the same end point, which are not stable. Very recently, the concept of topological-phonon-mediated superconductivity has been proposed[67]. It is a kind of *boundary superconductivity* that the electrons are mediated by the nontrivial surface/edge phonon modes, promising for a strong EPC[68]. In this sense, the one-dimensional zigzag ribbons of ZrCl or MoCl are potential for further realizing an edge-enhanced EPC or superconductivity than the 2D bulk, for the following reasons: (1) The TES contributed DOS are much larger than the bulk; (2) The TES has a w-shape (i.e., two-dip like) dispersion, which is favorable for the electron-phonon interaction.

DISCUSSION

In summary, we have predicted the phonon-mediated superconductivity and topological aspects in vdW-monolayered *MX* (M = Zr, Mo; X = F, Cl). We highlight that the 2D *MX* family host remarkable T_c, arising from the soft-mode-enhanced EPC. Particularly, monolayer MoCl displays a striking two-gap superconductivity because of disparate pairing strengths at each FS sheet. We have also discussed about the interesting Janus monolayer Zr_2FCl, which has the inversion breaking with respect to monolayer ZrCl. The discovered T_c-enhancement may facilitate the study of chiral-phonon-related superconductivity. Moreover, the electronic and phononic topology of 2D *MX* have been inspected. We demonstrate that monolayer MoF and MoCl are TSC candidates, and there exist Dirac phonons at Brillouin zone boundaries of monolayer ZrCl and MoCl. Our findings enrich the 2D superconducting and topological states in a single material platform.

METHODS

Electronic and phononic properties

We performed first-principles calculations via QUANTUM ESPRESSO package[69] with relativistic norm-conserving ONCV pseudopotentials[70]. The Perdew-Bruke-Ernzerhof exchange-correlation functional[71] of generalized gradient approximation was adopted. We employed a plane-wave cutoff energy of 120 Ry and a force tolerance of 1.0×10^{-4} Ry Å^{-1} under atomic relaxations. An k-mesh of $24 \times 24 \times 1$ and a Marzari-Vanderbilt smearing of 0.01 Ry were adopted for the monolayer structures. Electronic nesting function $\chi''(\mathbf{q})$ was calculated using a dense $200 \times 200 \times 1$ k-mesh, where $\chi''(\mathbf{q})$ is obtained by[72]

$$\chi''(\mathbf{q}) = \sum_{\mathbf{k}} \delta(\varepsilon_{\mathbf{k}} - E_F)\delta(\varepsilon_{\mathbf{k}+\mathbf{q}} - E_F). \quad (1)$$

The dynamical matrices and EPC matrices were computed by density functional perturbation theory with spin-orbit coupling. A q-mesh of $6 \times 6 \times 1$ was chosen for the monolayers. We constructed maximally localized Wannier functions[73] from d orbitals of Zr (Mo) atoms and p orbitals of Cl (F) atoms using Wannier90 code[74]. We generated the phononic tight-binding Hamiltonians by phonopyTB code[75]. The electronic and phononic edge spectra were calculated by the iterative Green's function technique[76], as implemented in WannierTools package[75].

Superconducting properties

Under convergence tests (Supplementary Note 1), we employed an EPC matrix interpolation to the denser $72 \times 72 \times 1$ k-mesh and $72 \times 72 \times 1$ q-mesh via the EPW code[77]. Then the Eliashberg spectral function $a^2F(\omega)$ was calculated by[78]

$$a^2F(\omega) = \frac{1}{2\pi N(E_F)} \sum_{\mathbf{q}\nu} \frac{\gamma_{\mathbf{q}\nu}}{\omega_{\mathbf{q}\nu}} \delta(\omega - \omega_{\mathbf{q}\nu}), \quad (2)$$

where $\gamma_{\mathbf{q}\nu}$ is the phonon linewidth and $\omega_{\mathbf{q}\nu}$ is the phonon eigen frequency. The EPC constant λ was obtained from the integral of $a^2F(\omega)$ by

$$\lambda = 2\int_0^\infty \frac{a^2F(\omega)}{\omega} d\omega. \quad (3)$$

The critical superconducting temperature T_c was estimated using McMillan-Allen-Dynes formula[49]:

$$T_c = \frac{\omega_{log}}{1.2} \exp\left(-\frac{1.04(1+\lambda)}{\lambda - \mu^*(1+0.62\lambda)}\right), \quad (4)$$

where ω_{log} is a logarithmic average of the phonon frequency and μ^* is the effective Coulomb repulsion constant, which typically values between 0.05 and 0.2. We adopted $\mu^* = 0.1$ for predicting T_c, as widely used in other 2D materials[17,24,79]. We also calculated the superconducting properties of monolayer ZrCl and MoCl by directly solving anisotropic (isotropic) Migdal-Eliashberg equations[53] provided by EPW code. The electronic states between $E_F - 0.8$ eV and $E_F + 0.8$ eV were taken into account and the Matsubara frequency cutoff was set as 0.2 eV. The delta smearing was 25 meV for electrons and 0.05 meV for EPC sum-over.

DATA AVAILABILITY

The data supporting the findings of this paper are available from the corresponding author upon reasonable request.

CODE AVAILABILITY

The central codes used in this paper are QUANTUM ESPRESSO, EPW, Wannier90, and WannierTools. Detailed information related to the license and user guide for these codes are available at https://www.quantum-espresso.org, https://docs.epw-code.org, http://www.wannier.org and http://www.wanniertools.com.

Received: 22 January 2022; Accepted: 8 August 2022;
Published online: 30 August 2022

REFERENCES

1. Saito, Y., Nojima, T. & Iwasa, Y. Highly crystalline 2D superconductors. *Nat. Rev. Mater.* **2**, 16094 (2016).
2. Brun, C., Cren, T. & Roditchev, D. Review of 2D superconductivity: the ultimate case of epitaxial monolayers. *Supercond. Sci. Technol.* **30**, 013003 (2016).
3. Zhang, T. et al. Superconductivity in one-atomic-layer metal films grown on Si(111). *Nat. Phys.* **6**, 104–108 (2010).
4. Xu, C. et al. Large-area high-quality 2D ultrathin Mo_2C superconducting crystals. *Nat. Mater.* **14**, 1135–1141 (2015).
5. Liao, M. et al. Superconductivity in few-layer stanene. *Nat. Phys.* **14**, 344–348 (2018).
6. Xi, X. et al. Ising pairing in superconducting $NbSe_2$ atomic layers. *Nat. Phys.* **12**, 139–143 (2016).
7. Liu, Y. et al. Observation of in-plane quantum Griffiths singularity in two-dimensional crystalline superconductors. *Phys. Rev. Lett.* **127**, 137001 (2021).
8. Fisher, M. P. A. Quantum phase transitions in disordered two-dimensional superconductors. *Phys. Rev. Lett.* **65**, 923–926 (1990).
9. Yang, C. et al. Intermediate bosonic metallic state in the superconductor-insulator transition. *Science* **366**, 1505–1509 (2019).
10. Lu, J. et al. Evidence for two-dimensional Ising superconductivity in gated MoS_2. *Science* **350**, 1353–1357 (2015).
11. Tan, S. et al. Interface-induced superconductivity and strain-dependent spin density waves in FeSe/$SrTiO_3$ thin films. *Nat. Mater.* **12**, 634–640 (2013).
12. Ge, J.-F. et al. Superconductivity above 100 K in single-layer FeSe films on doped $SrTiO_3$. *Nat. Mater.* **14**, 285–289 (2015).
13. Bekaert, J. et al. Hydrogen-induced high-temperature superconductivity in two-dimensional materials: the example of hydrogenated monolayer MgB_2. *Phys. Rev. Lett.* **123**, 077001 (2019).
14. Rhodes, D. A. et al. Enhanced superconductivity in monolayer T_d-$MoTe_2$. *Nano Lett.* **21**, 2505–2511 (2021).

15. Cheng, C. et al. Suppressed superconductivity in substrate-supported β_{12} borophene by tensile strain and electron doping. *2D Mater.* **4**, 025032 (2017).
16. Feng, B. et al. Experimental realization of two-dimensional boron sheets. *Nat. Chem.* **8**, 563–568 (2016).
17. Gao, M., Li, Q. Z., Yan, X. W. & Wang, J. Prediction of phonon-mediated superconductivity in borophene. *Phys. Rev. B* **95**, 024505 (2017).
18. Lian, C.-S., Si, C. & Duan, W. Unveiling charge-density wave, superconductivity, and their competitive nature in two-dimensional $NbSe_2$. *Nano Lett.* **18**, 2924–2929 (2018).
19. Zheng, F., Zhou, Z., Liu, X. & Feng, J. First-principles study of charge and magnetic ordering in monolayer $NbSe_2$. *Phys. Rev. B* **97**, 081101 (2018).
20. Liu, Y. et al. Type-II Ising superconductivity and anomalous metallic state in macro-size ambient-stable ultrathin crystalline films. *Nano Lett.* **20**, 5728–5734 (2020).
21. Wang, C. et al. Type-II Ising superconductivity in two-dimensional materials with spin-orbit coupling. *Phys. Rev. Lett.* **123**, 126402 (2019).
22. Yoshida, M., Kudo, K., Nohara, M. & Iwasa, Y. Metastable superconductivity in two-dimensional $IrTe_2$ crystals. *Nano Lett.* **18**, 3113–3117 (2018).
23. Fang, Y. et al. Discovery of superconductivity in 2M WS_2 with possible topological surface states. *Adv. Mater.* **31**, 1901942 (2019).
24. Campi, D., Kumari, S. & Marzari, N. Prediction of phonon-mediated superconductivity with high critical temperature in the two-dimensional topological semimetal W_2N_3. *Nano Lett.* **21**, 3435–3442 (2021).
25. You, J.-Y., Gu, B., Su, G. & Feng, Y. P. Two-dimensional topological superconductivity candidate in a van der Waals layered material. *Phys. Rev. B* **103**, 104503 (2021).
26. Wang, Z. et al. Topological edge states in a high-temperature superconductor FeSe/$SrTiO_3$(001) film. *Nat. Mater.* **15**, 968–973 (2016).
27. Alicea, J. New directions in the pursuit of Majorana fermions in solid state systems. *Rep. Prog. Phys.* **75**, 076501 (2012).
28. Fu, L. & Kane, C. L. Superconducting proximity effect and Majorana fermions at the surface of a topological insulator. *Phys. Rev. Lett.* **100**, 096407 (2008).
29. Lüpke, F. et al. Proximity-induced superconducting gap in the quantum spin Hall edge state of monolayer WTe_2. *Nat. Phys.* **16**, 526–530 (2020).
30. Kezilebieke, S. et al. Topological superconductivity in a van der Waals heterostructure. *Nature* **588**, 424–428 (2020).
31. Hor, Y. S. et al. Superconductivity in $Cu_xBi_2Se_3$ and its implications for pairing in the undoped topological insulator. *Phys. Rev. Lett.* **104**, 057001 (2010).
32. Sasaki, S. et al. Topological Superconductivity in $CuxBi_2Se_3$. *Phys. Rev. Lett.* **107**, 217001 (2011).
33. Sajadi, E. et al. Gate-induced superconductivity in a monolayer topological insulator. *Science* **362**, 922–925 (2018).
34. Kirshenbaum, K. et al. Pressure-induced unconventional superconducting phase in the topological insulator Bi_2Se_3. *Phys. Rev. Lett.* **111**, 087001 (2013).
35. Wang, M.-X. et al. The coexistence of superconductivity and topological order in the Bi_2Se_3 thin films. *Science* **336**, 52–55 (2012).
36. Lv, Y.-F. et al. Experimental signature of topological superconductivity and Majorana zero modes on β-Bi_2Pd thin films. *Sci. Bull.* **62**, 852–856 (2017).
37. Jin, K.-H. et al. Topological superconducting phase in high-T_c superconductor MgB_2 with Dirac-nodal-line fermions. *NPJ Comput. Mater.* **5**, 57 (2019).
38. Yuan, Y. et al. Evidence of anisotropic Majorana bound states in 2M-WS_2. *Nat. Phys.* **15**, 1046–1051 (2019).
39. Zhang, S. et al. Role of $SrTiO_3$ phonon penetrating into thin FeSe films in the enhancement of superconductivity. *Phys. Rev. B* **94**, 081116 (2016).
40. Li, J. et al. Computation and data driven discovery of topological phononic materials. *Nat. Commun.* **12**, 1–12 (2021).
41. Li, R. et al. Underlying topological Dirac Nodal line mechanism of the anomalously large electron-phonon coupling strength on a Be (0001) surface. *Phys. Rev. Lett.* **123**, 136802 (2019).
42. Lian, C.-S., Si, C. & Duan, W. Anisotropic full-Gap superconductivity in 2M-WS_2 topological metal with intrinsic proximity effect. *Nano Lett.* **21**, 709–715 (2020).
43. Bardeen, J., Cooper, L. N. & Schrieffer, J. R. Theory of superconductivity. *Phys. Rev.* **108**, 1175 (1957).
44. Adolphson, D. G. & Corbett, J. D. Crystal structure of zirconium monochloride. A novel phase containing metal-metal bonded sheets. *Inorg. Chem.* **15**, 1820–1823 (1976).
45. Struss, A. W. & Corbett, J. D. Lower chlorides of zirconium and hafnium. Formation of stable monochlorides. *Inorg. Chem.* **9**, 1373–1376 (1970).
46. Claassen, H. H., Goodman, G. L., Holloway, J. H. & Selig, H. Raman spectra of MoF_6, TcF_6, ReF_6, UF_6, SF_6, SeF_6, and TeF_6 in the vapor state. *J. Chem. Phys.* **53**, 341–348 (1970).
47. Grimme, S., Antony, J., Ehrlich, S. & Krieg, H. A consistent and accurate ab initio parametrization of density functional dispersion correction (DFT-D) for the 94 elements H-Pu. *J. Chem. Phys.* **132**, 154104 (2010).
48. Mounet, N. et al. Two-dimensional materials from high-throughput computational exfoliation of experimentally known compounds. *Nat. Nanotechnol.* **13**, 246–252 (2018).
49. Allen, P. B. & Dynes, R. Transition temperature of strong-coupled superconductors reanalyzed. *Phys. Rev. B* **12**, 905 (1975).
50. Zhang, L. & Niu, Q. Chiral phonons at high-symmetry points in monolayer hexagonal lattices. *Phys. Rev. Lett.* **115**, 115502 (2015).
51. Chomaz, L. et al. Observation of roton mode population in a dipolar quantum gas. *Nat. Phys.* **14**, 442–446 (2018).
52. Kishine, J., Ovchinnikov, A. S. & Tereshchenko, A. A. Chirality-induced phonon dispersion in a noncentrosymmetric micropolar crystal. *Phys. Rev. Lett.* **125**, 245302 (2020).
53. Margine, E. R. & Giustino, F. Anisotropic Migdal-Eliashberg theory using Wannier functions. *Phys. Rev. B* **87**, 024505 (2013).
54. Johnston, D. C. Elaboration of the α-model derived from the BCS theory of superconductivity. *Supercond. Sci. Technol.* **26**, 115011 (2013).
55. Choi, H. J. et al. The origin of the anomalous superconducting properties of MgB_2. *Nature* **418**, 758–760 (2002).
56. Gurevich, A. et al. Very high upper critical field in the two-gap superconductor MgB_2 produced by selective tuning of impurity scattering. *Supercond. Sci. Technol.* **17**, 278 (2003).
57. Kohn, W. Image of the fermi surface in the vibration spectrum of a metal. *Phys. Rev. Lett.* **2**, 393–394 (1959).
58. Katsnelson, M. I., Naumov, I. I. & Trefilov, A. V. Singularities of the electronic structure and pre-martensitic anomalies of lattice properties in β-phases of metals and alloys. *Phase Transit.* **49**, 143–191 (1994).
59. Katsnelson, M. I. & Trefilov, A. V. Anomalies caused in phonon spectra by charge density fluctuations. *JETP Lett.* **42**, 485 (1985).
60. Heil, C. et al. Origin of superconductivity and latent charge density wave in NbS_2. *Phys. Rev. Lett.* **119**, 087003 (2017).
61. Tse, J. S., Yao, Y. & Tanaka, K. Novel superconductivity in metallic SnH_4 under high pressure. *Phys. Rev. Lett.* **98**, 117004 (2007).
62. Giustino, F. Electron-phonon interactions from first principles. *Rev. Mod. Phys.* **89**, 015003 (2017).
63. Wang, Z. et al. Topological nature of the $FeSe_{0.5}Te_{0.5}$ superconductor. *Phys. Rev. B* **92**, 115119 (2015).
64. Song, Z., Zhang, T., Fang, Z. & Chen, F. Quantitative mappings between symmetry and topology in solids. *Nat. Commun.* **9**, 3530 (2018).
65. Zhang, R.-X. & Das Sarma, S. Intrinsic time-reversal-invariant topological superconductivity in thin films of iron-based superconductors. *Phys. Rev. Lett.* **126**, 137001 (2021).
66. Li, J. et al. Topological phonons in graphene. *Phys. Rev. B* **101**, 081403 (2020).
67. Di Miceli, D., Setty C. & Zaccone A. Theory of superconductivity mediated by topological phonons. *Phys. Rev. B* **106**, 054502 (2022).
68. Atta-Fynn, R., Biswas, P. & Drabold, D. A. Electron-phonon coupling is large for localized states. *Phys. Rev. B* **69**, 245204 (2004).
69. Giannozzi, P. et al. QUANTUM ESPRESSO: a modular and open-source software project for quantum simulations of materials. *J. Phys. Condens. Matter* **21**, 395502 (2009).
70. Schlipf, M. & Gygi, F. Optimization algorithm for the generation of ONCV pseudopotentials. *Comput. Phys. Commun.* **196**, 36–44 (2015).
71. Perdew, J. P., Burke, K. & Ernzerhof, M. Generalized gradient approximation made simple. *Phys. Rev. Lett.* **77**, 3865–3868 (1996).
72. Johannes, M. & Mazin, I. Fermi surface nesting and the origin of charge density waves in metals. *Phys. Rev. B* **77**, 165135 (2008).
73. Marzari, N. & Vanderbilt, D. Maximally localized generalized Wannier functions for composite energy bands. *Phys. Rev. B* **56**, 12847 (1997).
74. Mostofi, A. A. et al. An updated version of wannier90: a tool for obtaining maximally-localised Wannier functions. *Comput. Phys. Commun.* **185**, 2309–2310 (2014).
75. Wu, Q. S. et al. WannierTools: An open-source software package for novel topological materials. *Comput. Phys. Commun.* **224**, 405–416 (2018).
76. Sancho, M. P. L., Sancho, J. M. L. & Rubio, J. Highly convergent schemes for the calculation of bulk and surface Green functions. *J. Phys. F.* **15**, 851–858 (1985).
77. Poncé, S., Margine, E. R., Verdi, C. & Giustino, F. EPW: Electron–phonon coupling, transport and superconducting properties using maximally localized Wannier functions. *Comput. Phys. Commun.* **209**, 116–133 (2016).
78. Baroni, S., De Gironcoli, S., Dal Corso, A. & Giannozzi, P. Phonons and related crystal properties from density-functional perturbation theory. *Rev. Mod. Phys.* **73**, 515 (2001).
79. Profeta, G., Calandra, M. & Mauri, F. Phonon-mediated superconductivity in graphene by lithium deposition. *Nat. Phys.* **8**, 131–134 (2012).

ACKNOWLEDGEMENTS

This work was supported by the National Key Research and Development Program of China (Grant Nos. 2020YFA0308800), the National Natural Science Foundation of China (Grant No. 11974045, 61888102), Chinese Academy of Sciences (Grant Nos. XDB30000000), CAS Project for Young Scientists in Basic Research (YSBR-003), Beijing Institute of Technology Research Fund Program for Young Scholars (Grants No. 3050011181909) and the Fundamental Research Funds for the Central Universities. F.L. was supported by DOE-BES (Grant No. DE-FG02-04ER46148). Computational resources were provided by the National Superconducting Center in Guangzhou.

AUTHOR CONTRIBUTIONS

S.D. and F.L. conceived and coordinated the research project. W.-H.D. performed the first-principles calculations and data analysis. W.-H.D. wrote the intial manuscript. All authors participated in discussing and editing the manuscript.

COMPETING INTERESTS

The authors declare no competing interests.

ADDITIONAL INFORMATION

Supplementary information The online version contains supplementary material available at https://doi.org/10.1038/s41524-022-00871-y.

Correspondence and requests for materials should be addressed to Feng Liu or Shixuan Du.